Hydrology and
Earth System
Sciences

Open Access

EGU

Supplement of

Technical note: Testing the effect of different pumping rates on pore-water sampling for ions, stable isotopes, and gas concentrations in the hyporheic zone

Tamara Michaelis et al.

Correspondence to: Florian Einsiedl (f.einsiedl@tum.de)

Supplement

S1 Sediment properties

For sediment characterization, cores were taken by manually pushing a liner with 6 cm inner diameter into the sediment. In September 2021 and August 2022 sieve-slurry analyses were performed, each time for two homogeneous layers, according to the German norm DIN 17892-4. Resulting grain-size distribution curves are displayed in Fig. S1. Porosity was measured
5   from two separate liners by weighting a known volume of sediment before and after drying at 105 °C. The same samples were later used for the determination of organic carbon content as Loss On Ignition (LOI) according to the German DIN 18128. After grinding and weighting, samples were annealed in a furnace at 550 °C to constant mass, cooled to room temperature in a desiccator, and weighted again. Results showed that the sediment at the sampling site consisted of 3 % gravel, 27 % sand and 70 % silt with a porosity of 81.5 % and an LOI of 21 %.
10   Three additional cores were used for measurements of thermal conductivity with the TCi-3-A Thermal Conductivity Analyzer and a Transient Line Source (TLS) (C-Therm, Fredericton, Canada). The sediment cores were taken in liners with 42 cm diameter and sample heights between 25 and 30 cm. Measurements were conducted at a constant temperature of 8±1°C, close to true sediment temperatures, in a cooling room, and samples were pre-tempered for >12 hours. The line source with a sensor length of 15 cm was inserted vertically in the center of the sediment core and heated with 0.1 W. In most measurements, small
15   deviations from the expected linear relation between the logarithm of time and the change in measured temperature were observed. Linear regression reached $R^2 = 0.972$ to 0.984. Most likely, this was caused by inhomogeneities in the sample or small rates of water drainage and consolidation during the measurement. Values for thermal conductivity λ between 0.56 and 0.64 W m^{-1} K^{-1} were found. In this study, we used the median $\lambda = 0.60$ W m^{-1} K^{-1}. This value lies well in the range of 0.20 to 0.70 W m^{-1} K^{-1} (mean: 0.51 W m^{-1} K^{-1}) found by Dalla Santa et al. (2020) for unconsolidated material with an organic
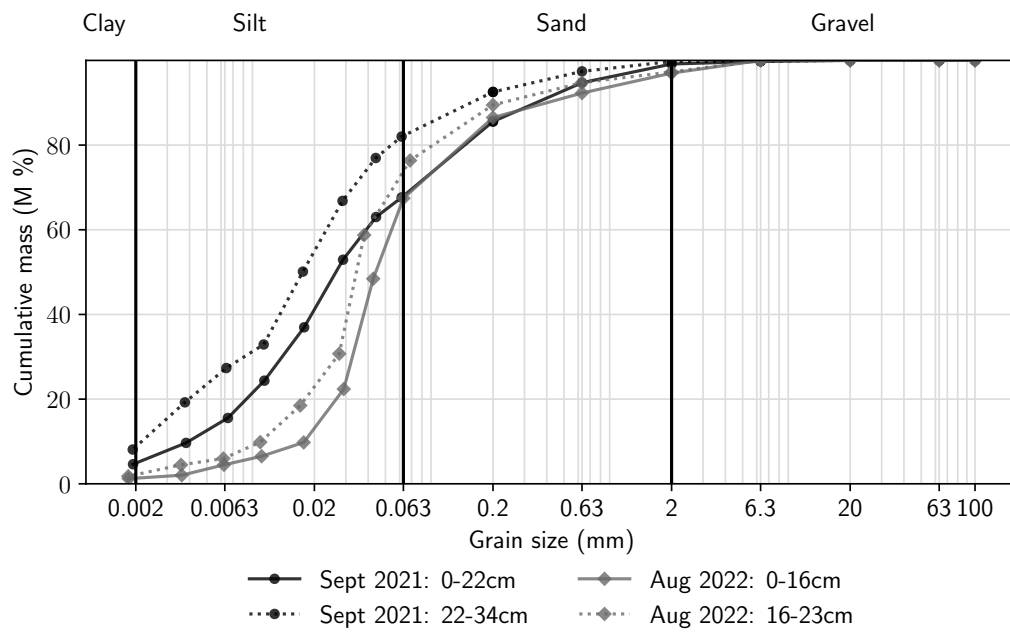20   matter content of >5%.

Figure S1. Grain-size distribution curves from sediment cores taken in September 2021 and August 2022.

S2 Geochemistry of the sampling site

Dates, sampling method and pumping rate for all sampling campaigns are summarized in Tab. S1. During 11 sampling campaigns between April and September 2021, samples were withdrawn with two LA-110 High Pressure syringe pumps (HLL Landgraf Laborsysteme, Langenhausen, Deutschland) at a pumping rate of $0.15 \, \text{mL} \, \text{min}^{-1}$. The syringe pumps were equipped with 3D printed racks to hold 5 syringes each. Thus, up to 10 samples could be withdrawn simultaneously. Samples were collected in the syringes and then transferred to the respective vials for gas, sulfide, anion, or cation analyses. However, several disadvantages became obvious during sampling: not all 15 Rhizon samplers could be sampled simultaneously, thus making cross-contamination of samples from different depths more likely; syringes filled at different speeds, potentially due to sediment heterogeneities and gas intrusions; long stay of the sample in the syringes during collection made gas losses more likely. Therefore, the sampling technique was improved in 2022 as described in the main text.

Sample collection was carried out as described in Sec. 2.1.1. For gas sampling with syringe pumps, two needles were pierced through the rubber stoppers for sample injection, one connected to the syringe and one for pressure exchange. Samples were injected slowly along the side of the vial to prohibit degassing. Both needles were removed directly after sampling.

Table S1. Summary of sampling dates, measurement technique and pumping rate.

| Date	Sampling technique	Pumping rate
19-04-2021		
10-05-2021		
26-05-2021		
09-06-2021		
23-06-2021	Rhizon samplers + syringe	
06-07-2021	pumps with space for max. 10	$0.15 \, \text{mL} \, \text{min}^{-1}$
20-07-2021	plastic syringes	
03-08-2021		
17-08-2021		
01-09-2021		
23-09-2021		
23-09-2021	Peeper	-
03-05-2022		
03-05-2022	Rhizon samplers + peristaltic	$0.19 \, \text{mL} \, \text{min}^{-1}$
30-05-2022	pumps (15 ports) and gastight	$0.09 \, \text{mL} \, \text{min}^{-1}$
31-05-2022	tubing	$0.38 \, \text{mL} \, \text{min}^{-1}$
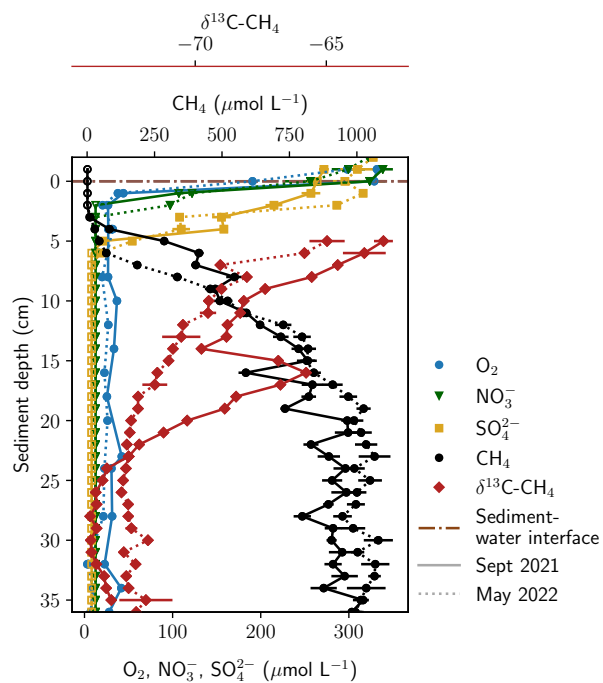
Figure S2. Comparison of two depth-profiles measured with pore-water dialysis samplers (peepers) in September 2021 and May 2022.
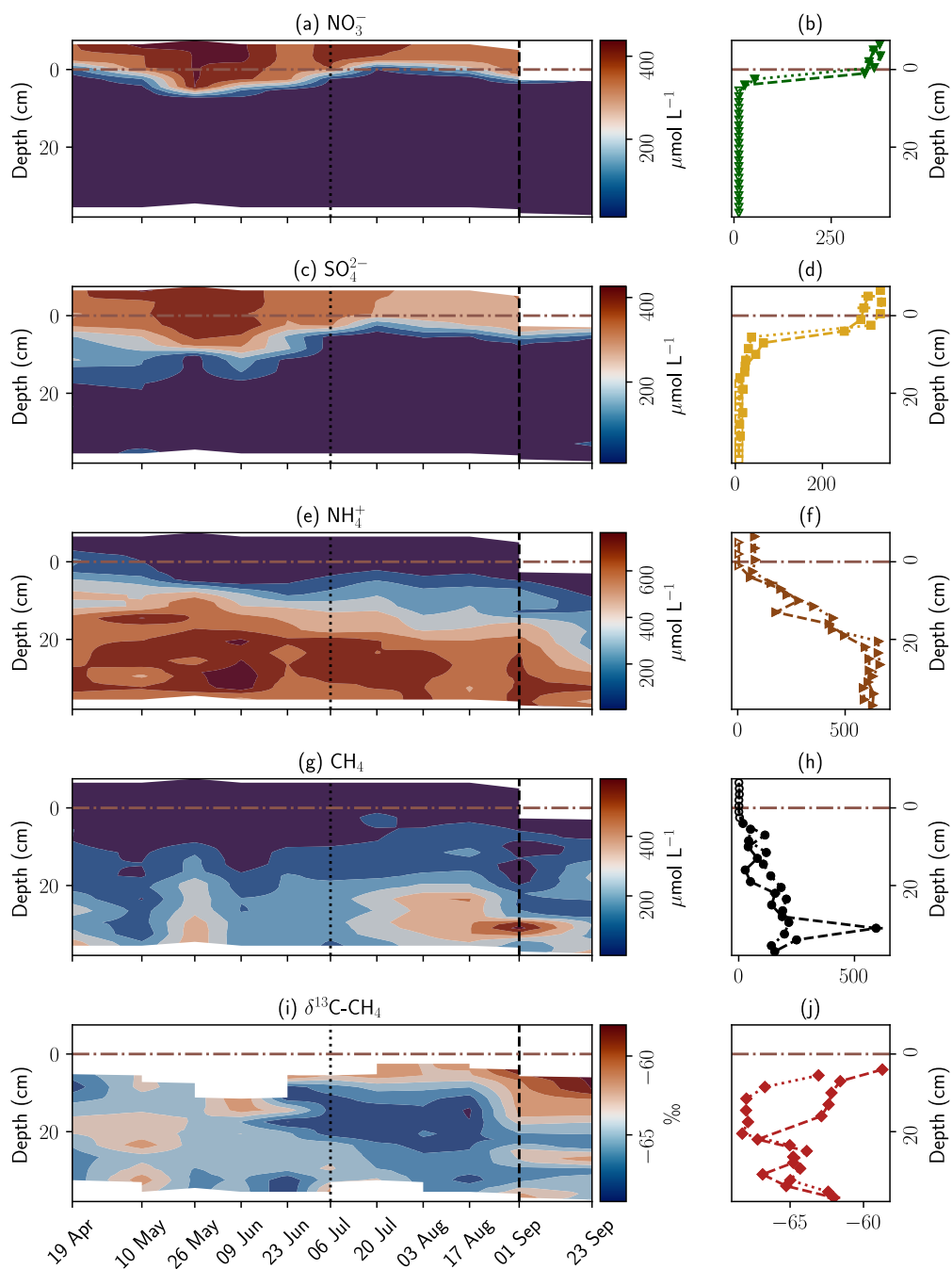
Figure S3. Concentration- and stable isotope measurements conducted at the monitoring station during spring and summer 2021. Panels on the left show concentrations over time as contour plots. Panels on the right show two selected depth-profiles.

S3 Oxygen sensor calibration

35   Calculation of dissolved O_2 concentrations from measured phase angles was based on the two-site quenching model of the Stern-Volmer equation (Eq. S1) (Carraway et al., 1991; Vieweg et al., 2013).

$$\frac{tan(\phi)}{tan(\phi_0)} = \frac{f}{1 + K_{SV}[O_2]} + \frac{1 - f}{1 + mK_{SV}[O_2]} \tag{S1}$$

with ϕ being the measured phase angle, ϕ_0 the phase angle at 0% a.s., K_{SV} the quenching constant as a function of saturation O_2 concentration, and f and m fit paramters. The parameters f, m, and K_{SV} (20 °C, lab air pressure) were estimated as best fit

40   for calibration measurements conducted at 7 different dissolved O_2 concentrations at 20 °C (Fig. S4 (a)).

Measured phase angles are temperature-dependent, thus compensation for field temperatures was necessary (Vieweg et al., 2013). For this, measurements were conducted at 0 % a.s. and 100 % a.s. at five and four environmentally relevant temperatures between 5 and 25 °C. The change of measured phase angle per Kelvin $\Delta\phi K_{\phi_0}^{-1}$ and $\Delta\phi K_{\phi_{100}}^{-1}$ at 0 % a.s. and 100 % a.s., respectively, was estimated with linear regression (Eq. S2, S3 and Fig. S4b).
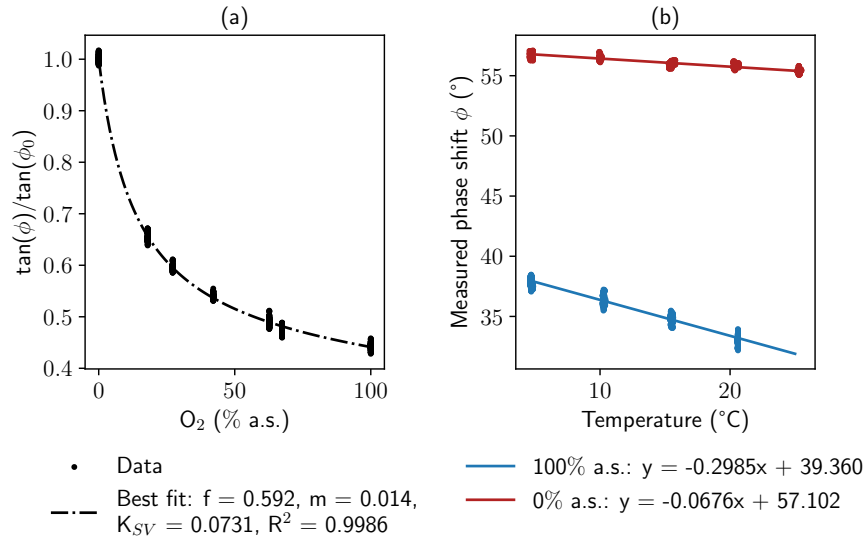

Figure S4. Calibration of the custom-made fiber-optical oxygen sensor. Panel (a) shows the Stern-Volmer Plot with best-fit parameters for the model and panel (b) the temperature dependence at 0 % and 100 % a.s.

45    $$tan(\phi_0)[T_m] = tan(\phi_0 + \Delta\phi K_{\phi_0}^{-1}(T_m - T_0)) \tag{S2}$$

$$tan(\phi_{100})[T_m] = tan(\phi_{100} + \Delta\phi K_{\phi_{100}}^{-1}(T_m - T_{100})) \tag{S3}$$

For the calculation of O_2 concentrations from phase angles measured in the field, first a fourth order polynomial was fit to temperature data recorded at the time of measurement to gain a continuous temperature depth-distribution (Fig. 4b). Above the sediment-water interface, average temperature of all sensors was assumed to be constant. For each depth, K_{SV} was re-calculated based on O_2 saturation concentration, a function of water temperature and pressure at the specific depth. Then, O_2 concentrations were calculated with the Stern-Volmer equation (Eq. S1) in % a.s. and converted to $\mu mol\,L^{-1}$ based on depth-dependent saturation concentrations.

Due to the flat shape of the calibration model in saturated and near-saturated conditions (Fig. 4a), small errors in measured phase angles partly led to extremely high concentrations. To avoid these unrealistic values, all concentrations of $>100\,\%$ a.s. were normalized such that the maximal concentration was $120\,\%$ a.s. (Eq. S4).

$$O_{2,nomalized} = \frac{20}{(O_{2,max} - 100)} \cdot (O_{2,original} - 100) + 100 \tag{S4}$$

where $O_{2,nomalized}$ is the normalized concentration value between $100\,\%$ and $120\,\%$ a.s., $O_{2,max}$ the maximally measured concentration considering all values of a profile, and $O_{2,original}$ the originally calculated concentration with an original value of $>100\,\%$ a.s.

S4   Additional pore-water analyses

This section includes additional information on pore-water sampling and analyses. The equilibration period of the peeper was between April 6th 2022 and May 3rd 2022. Rhizon sampling at $0.19\,\text{ml}\,\text{min}^{-1}$ was conducted on May 3rd right before sampling of the peeper. Pumping rates of $0.09\,\text{ml}\,\text{min}^{-1}$ and $0.38\,\text{ml}\,\text{min}^{-1}$ were tested on May 30th and 31st, respectively.

65 Box plots in Fig. S6 show that differences in Ca^{2+}, Mg^{2+}, and Cl^- concentrations were significant between samples withdrawn with the peeper and Rhizons. This difference may have been caused directly by the sampling technique or by small-scale chemical heterogeneities, because the peeper was placed approx. $15\,\text{cm}$ away from the monitoring station to avoid mutual disturbances. Box plots are also provided for CH_4 concentrations and $\delta^{13}C\text{-}CH_4$ in Fig. S5, as well as $\delta^{18}O$ and δ^2H in Fig. S7. Data sets of $\delta^{18}O$ and δ^2H were not significantly different for high and low pumping rates.
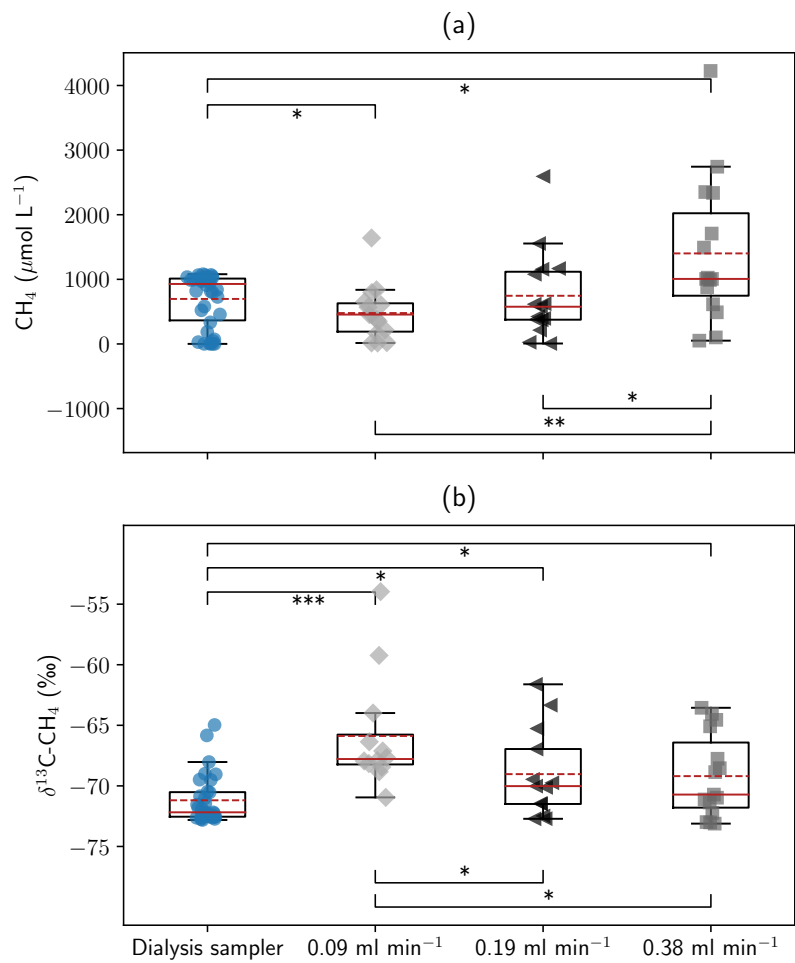
Figure S5. Box plots of (a) CH_4 concentration and (b) stable isotope measurements. The box indicates the inter-quartile range (IQR) between first and third quartile. Whiskers show 1.5 times the IQR. Median is displayed as solid, mean as dashed line. Where pairwise comparisons (Mann Whitney U test) showed significant differences, this is marked as follows: *(0.05 > p > 0.01), **(0.01 > p > 0.001), ***(p < 0.001).

Figure S6. Box plots of (a) Ca^{2+}, (b) Mg^{2+}, and (c) Cl^- concentration data. The box indicates the inter-qurtile range (IQR) between first and third quartile. Whiskers show 1.5 times the IQR. Median is displayed as solid, mean as dashed line. Where pairwise comparisons (Mann Whitney U test) showed significant differences, this is marked as follows: *(0.05 > p > 0.01), **(0.01 > p > 0.001), ***(p < 0.001).
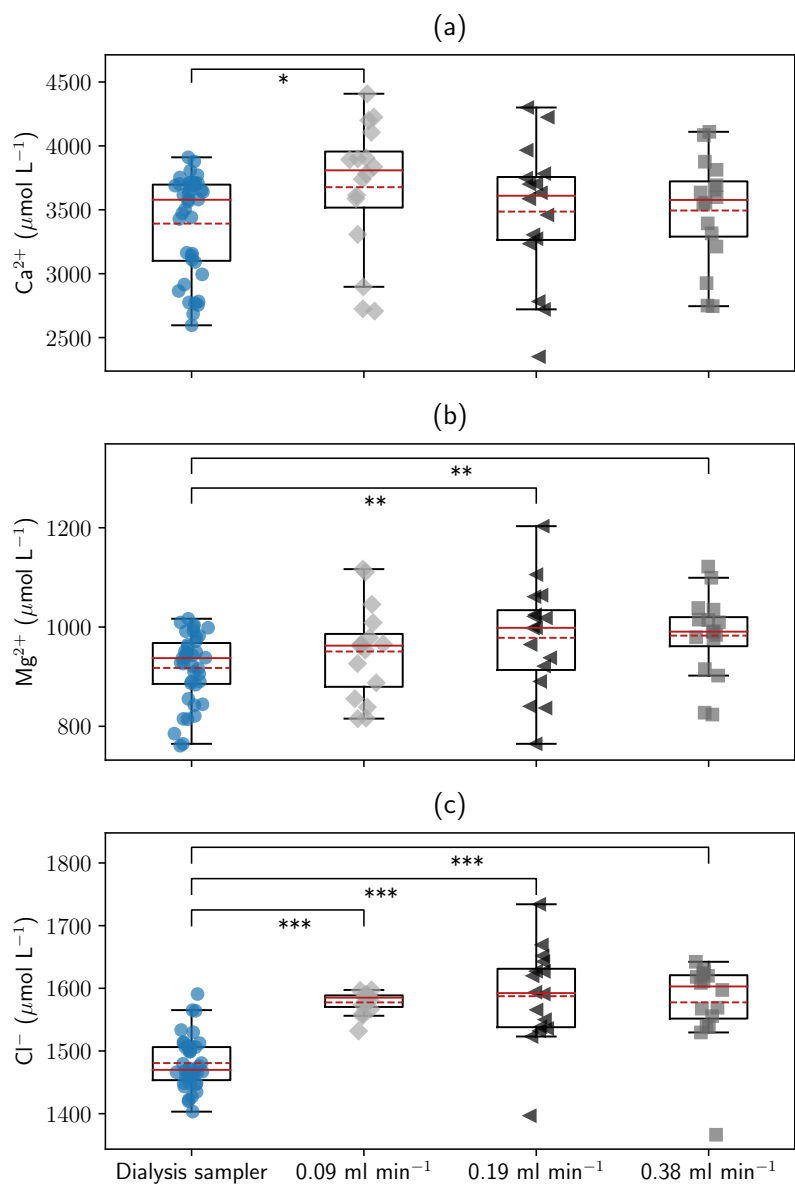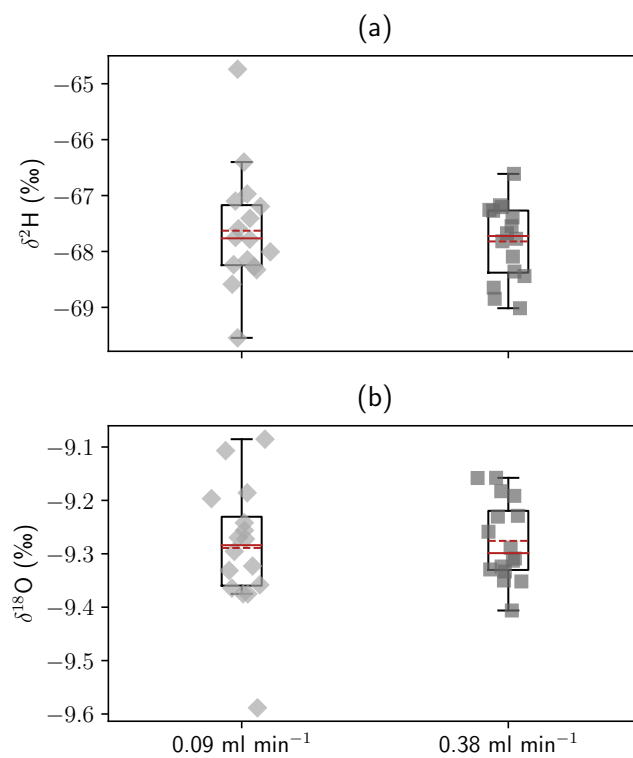
Figure S7. Box plots of (a) δ^2H, and (b) δ^{18}O data. The box indicates the inter-qurtile range (IQR) between first and third quartile. Whiskers show 1.5 times the IQR. Median is displayed as solid, mean as dashed line. Differences between the data sets were not significant.

S5 Detailed temperature modeling results

Flux rates calculated with both amplitude and phase methods by Hatch et al. (2006) and Keery et al. (2007) from the deepest 6 sensors in 6 cm, 8 cm, 10 cm, 12 cm, 14 cm, and 24 cm depth are given in Fig. S8. Fluxes were calculated between overlapping sensor pairs. For example, the flux calculated for 8 cm depth was calculated from the sensors in 6 cm and 10 cm depth. Mean, mean of absolute values, range, and the percentage of negative values for each simulated time series are summarized in Tab. S2. Based on the amplitude method, the majority of values was negative when considering sensors at 8 cm depth and deeper, indicating upwards directed flow. Values calculated for shallower depths were mainly positive, showing large peaks when considering sensors placed in less than 6 cm depth. These peaks are assumed to be caused by sediment dynamics like sedimentation and erosion (see main paper). With the phase method, only absolute flux rates could be calculated.

Fluxes calculated based on phase change were 4-18 times larger than fluxes based on amplitude dampening. Amplitude dampening was pronounced in the data while phase differences between the sensor pairs were only very small. In fact, it was not possible to get flux estimates from neighboring sensors with the phase method due to the minimal time lag which was smaller than the temporal resolution of the time series. Therefore, we hypothesize that for our data set estimates based on the amplitude method are much more reliable and have chosen not to display results based on the phase method in the main paper. The data is still displayed here to allow a comparison and for transparency by showing all results.

The influence of the thermal dispersivity parameter β was tested with a Monte Carlo analysis on a reduced data set, including data from April and May 2022 and the sensor pair in 8 cm and 12 cm depth. A normal distribution was assumed for the parameter β, with different means and standard deviations. For each scenario, 100 runs of VFLUX were performed with the random variations of β according to the respective distribution. The results show that higher thermal dispersion would lead to lower absolute flux values and less intense fluctuations (Fig. S9). Considering that β was changed by two orders of magnitude, the sensitivity of the model to changes in dispersivity appear to be limited. Nevertheless, further investigations on thermal dispersivity could help to improve the use of temperature measurements for hyporheic exchange flux modeling.
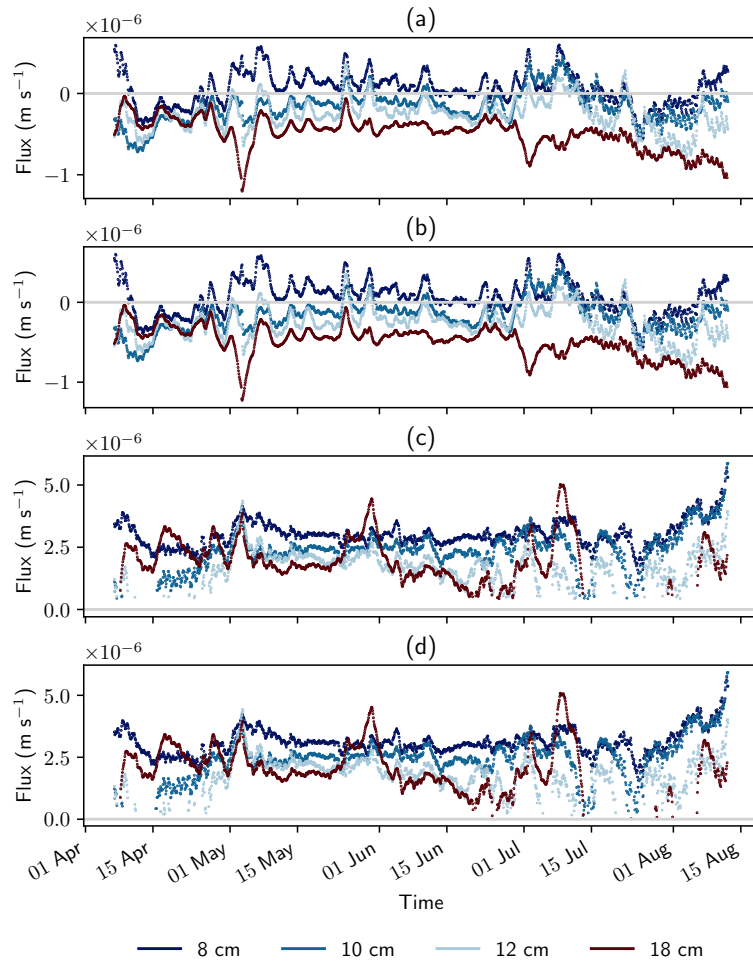
Figure S8. Detailed results of VFLUX modeling. Calculated fluxes are based on (a) amplitude method by Hatch et al. (2006), (b) amplitude method by Keery et al. (2007), (c) phase method by Hatch et al. (2006), and (d) phase method by Keery et al. (2007). Positive flow in (a) and (b) is downwards directed. The phase method in (c) and (d) only gives absolute values and no direction of flow.

Table S2. Summary of results from VFLUX modeling from sensors in $6\,\mathrm{cm}$, $8\,\mathrm{cm}$, $10\,\mathrm{cm}$, $12\,\mathrm{cm}$, $14\,\mathrm{cm}$, and $24\,\mathrm{cm}$ depths. Fluxes were calculated between each other sensor. For example, the flux calculated for $8\,\mathrm{cm}$ depth was calculated from the sensors in $6\,\mathrm{cm}$ and $10\,\mathrm{cm}$ depth. Lower sensors were not included due a strong influence of sedimentation and erosion events. All values are given in $\mathrm{m\,s^{-1}}$.

| Depth		Hatch amplitude	Keery amplitude	Hatch phase	Keery phase
8 cm	mean	$6.3 \cdot 10^{-8}$	$6.3 \cdot 10^{-8}$		
	mean (abs)	$1.7 \cdot 10^{-7}$	$1.7 \cdot 10^{-7}$	$3.0 \cdot 10^{-6}$	$3.1 \cdot 10^{-6}$
	range	$-5.6 \cdot 10^{-7}$ to $6.0 \cdot 10^{-7}$	$-5.7 \cdot 10^{-7}$ to $6.0 \cdot 10^{-7}$	$1.2 \cdot 10^{-6}$ to $5.7 \cdot 10^{-6}$	$1.3 \cdot 10^{-6}$ to $5.7 \cdot 10^{-6}$
	$\% < 0$	34%	34%	-	-
10 cm	mean	$-1.6 \cdot 10^{-7}$	$-1.6 \cdot 10^{-7}$		
	mean (abs)	$2.1 \cdot 10^{-7}$	$2.1 \cdot 10^{-7}$	$2.4 \cdot 10^{-6}$	$2.5 \cdot 10^{-6}$
	range	$-7.2 \cdot 10^{-7}$ to $4.5 \cdot 10^{-7}$	$-7.3 \cdot 10^{-7}$ to $4.6 \cdot 10^{-7}$	$4.4 \cdot 10^{-7}$ to $5.8 \cdot 10^{-6}$	$1.5 \cdot 10^{-7}$ to $5.9 \cdot 10^{-6}$
	$\% < 0$	85%	85%	-	-
12 cm	mean	$-2.6 \cdot 10^{-7}$	$-2.6 \cdot 10^{-7}$		
	mean (abs)	$2.8 \cdot 10^{-7}$	$2.8 \cdot 10^{-7}$	$1.8 \cdot 10^{-6}$	$1.9 \cdot 10^{-6}$
	range	$-7.9 \cdot 10^{-7}$ to $3.4 \cdot 10^{-7}$	$-8.1 \cdot 10^{-7}$ to $3.5 \cdot 10^{-7}$	$4.3 \cdot 10^{-7}$ to $4.4 \cdot 10^{-6}$	$1.7 \cdot 10^{-7}$ to $4.4 \cdot 10^{-6}$
	$\% < 0$	90%	90%	-	-
18 cm	mean	$-4.9 \cdot 10^{-7}$	$-5.0 \cdot 10^{-7}$		
	mean (abs)	$4.9 \cdot 10^{-7}$	$5.0 \cdot 10^{-7}$	$2.1 \cdot 10^{-6}$	$2.1 \cdot 10^{-6}$
	range	$-1.2 \cdot 10^{-6}$ to $-3.5 \cdot 10^{-8}$	$-1.2 \cdot 10^{-6}$ to $-3.5 \cdot 10^{-8}$	$4.3 \cdot 10^{-7}$ to $5.0 \cdot 10^{-6}$	$2.4 \cdot 10^{-8}$ to $5.1 \cdot 10^{-6}$
	$\% < 0$	100%	100%	-	-
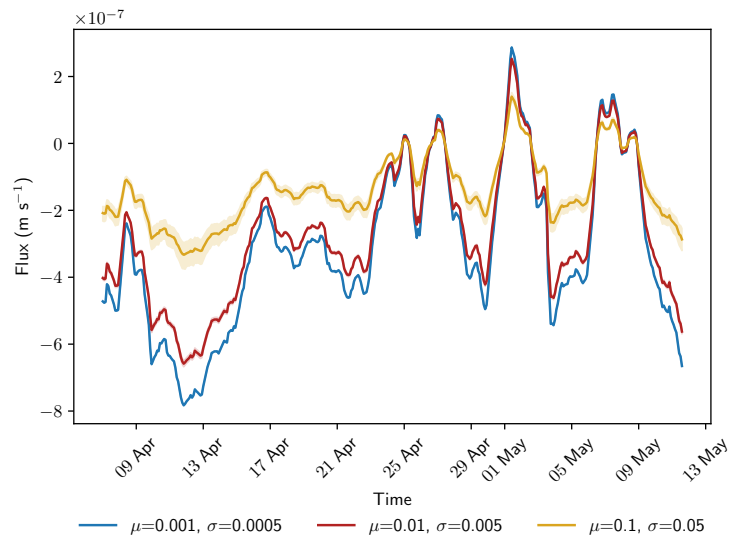
Figure S9. Monte Carlo analysis for thermal dispersivity. Three scenarios were tested for mean μ and standard deviation σ of the thermal dispersivity parameter β in m. Results were generated with n=100 runs for each scenario. Shading indicates 95 % confidence intervals for each scenario. The results were calculated with the software package VFLUX and the Hatch amplitude method.

References

Carraway, E. R., Demas, J. N., DeGraff, B. A., and Bacon, J. R.: Photophysics and photochemistry of oxygen sensors based on luminescent transition-metal complexes, Analytical Chemistry, 63, 337–342, https://doi.org/10.1021/ac00004a007, 1991.

95 Dalla Santa, G., Galgaro, A., Sassi, R., Cultrera, M., Scotton, P., Mueller, J., Bertermann, D., Mendrinos, D., Pasquali, R., and Perego, R.: An updated ground thermal properties database for GSHP applications, Geothermics, 85, 101758, https://doi.org/10.1016/j.geothermics.2019.101758, 2020.

Hatch, C. E., Fisher, A. T., Revenaugh, J. S., Constantz, J., and Ruehl, C.: Quantifying surface water–groundwater interactions using time series analysis of streambed thermal records: Method development, Water Resources Research, 42, https://doi.org/10.1029/2005WR004787,
100 2006.

Keery, J., Binley, A., Crook, N., and Smith, J. W.: Temporal and spatial variability of groundwater–surface water fluxes: Development and application of an analytical method using temperature time series, Journal of Hydrology, 336, 1–16, https://doi.org/10.1016/j.jhydrol.2006.12.003, 2007.

Vieweg, M., Trauth, N., Fleckenstein, J. H., and Schmidt, C.: Robust Optode-Based Method for Measuring in Situ Oxygen Profiles in
105 Gravelly Streambeds, Environmental Science & Technology, 47, 9858–9865, https://doi.org/10.1021/es401040w, 2013.